

DNSS: Dual-Normal Space Sampling for 3D ICP Registration

Tsz-Ho Kwok

Abstract—Rigid registration is a fundamental process in many applications that require alignment of different datasets. *Iterative Closest Point* (ICP) is a widely used algorithm that iteratively finds point correspondences and updates the rigid transformation. One of the key variants of ICP to its success is the selection of points, which is directly related to the convergence and robustness of the ICP algorithm. Besides uniform sampling, there are a number of normal-based and feature-based approaches that consider normal, curvature, and/or other signals in the point selection. Among them, *Normal Space Sampling* (NSS) is one of the most popular techniques due to its simplicity and low computational cost. The rationale of NSS is to sample enough constraints to determine all the components of transformation, but this study finds that NSS actually can constrain the translational normal space only. This paper extends the fundamental idea of NSS and proposes *Dual-Normal Space Sampling* (DNSS) to sample points in both translational and rotational normal spaces. Compared with NSS, this approach has similar simplicity and efficiency without any need of additional information, but has a much better effectiveness. Experimental results show that DNSS can outperform the normal-based and feature-based methods in terms of convergence and robustness. For example, DNSS can achieve convergence from an orthogonal initial position while no other methods can achieve.

Note to Practitioners—ICP is commonly used to align different data to a same coordination system. While NSS is often used to speed up the alignment process by down-sampling the data uniformly in the normal-space. The implementation of NSS only has three steps: (1) construct a set of buckets in the normal-space; (2) put all points of the data into buckets based on their normal direction; and (3) uniformly pick points from all the buckets until the desired number of points are selected. The algorithm is simple and fast, so that it is still the common practice. However, the weakness of NSS comes from the reason that it cannot handle rotational uncertainties. In this paper, a new algorithm called DNSS is developed to constrain both translation and rotation at the same time by introducing a dual-normal space. With a new definition of the normal space, the algorithm complexity of DNSS is the same as that of NSS, and it can be readily implemented in all types of application that are currently using ICP. The experimental results show that DNSS has better efficiency, quality, and reliability than both normal-based and feature-based methods.

Index Terms—Iterative closest point (ICP), Fine Registration, Point Sampling, Point Selection, Normal Space

T.-H. Kwok is with the Department of Mechanical, Industrial and Aerospace Engineering, Concordia University, Montreal, QC H3G 1M8, Canada. E-mail: tszho.kwok@concordia.ca

I. INTRODUCTION

REGRISTRATION is a process to align three-dimensional (3D) shapes of either different parts of an object or two different but similar objects. It is a fundamental task in many applications in computer vision, object recognition, computer graphics, robotics, medical imaging, statistical learning, etc. This is also referred to as *scene-to-model registration* that finds a rigid-body transformation to align a model (\mathcal{M}) to a scene (\mathcal{S}). Model and scene are the aliases for two 3D shapes, where scene stands for the static one and model stands for the moving one. The registration can be formulated as minimizing this energy function

$$E(\mathbf{R}, \mathbf{t}) = \frac{1}{n} \sum_{i=1}^n d(\mathbf{R}\mathbf{p}_i + \mathbf{t}, \mathcal{S}), \quad (1)$$

where the model is represented by a set of sampling points $M = \{\mathbf{p}_i \in \mathcal{M}, i = 1 \dots n\}$, \mathbf{R} is a rotation matrix, \mathbf{t} is a translation vector, and the metric d measures the error of distance to \mathcal{S} . Many practical applications still rely on the *Iterative Closest Point* (ICP) algorithm for fine registration when an initial transformation is given. ICP can efficiently align two datasets by alternating between matching corresponding points and updating the rigid transformation. ICP has been widely applied in face recognition [1], robot navigation [2], autonomous driving [3], terrain mapping [4], etc. ICP has many different elements, which can be summarized into these categories: point selection, point matching, pair weighting, outlier removal, error metric, and energy minimization. In general, these steps are applied sequentially in an ICP process, but each step is performed only if necessary. Among which, point selection is usually performed for the sake of convergence and computational complexity. This is because indiscriminately using all the points for registration will inordinately slow down the ICP convergence or even find a wrong pose. For instance, using the full set for the two-dimensional (2D) teeth shape shown in Fig. 1 results in multiple local minimums of energy along the X -axis because of the repeated tooth patterns. It has been shown that ICP is a gradient descent method [5] and proved to converge monotonically to a local minimum [6], and thus the range of convergence for the full set is $(-50, 50)$ along X -axis (the width of a tooth is 100). If points are properly selected (e.g., by dual-normal space sampling), the range of convergence is extended even wider than $[-225, 255]$ along X -axis, i.e., only one global optimum. Although it may not be always possible to have only one global optimum in all motions, this paper focus on the category of point selection in ICP and aims to look

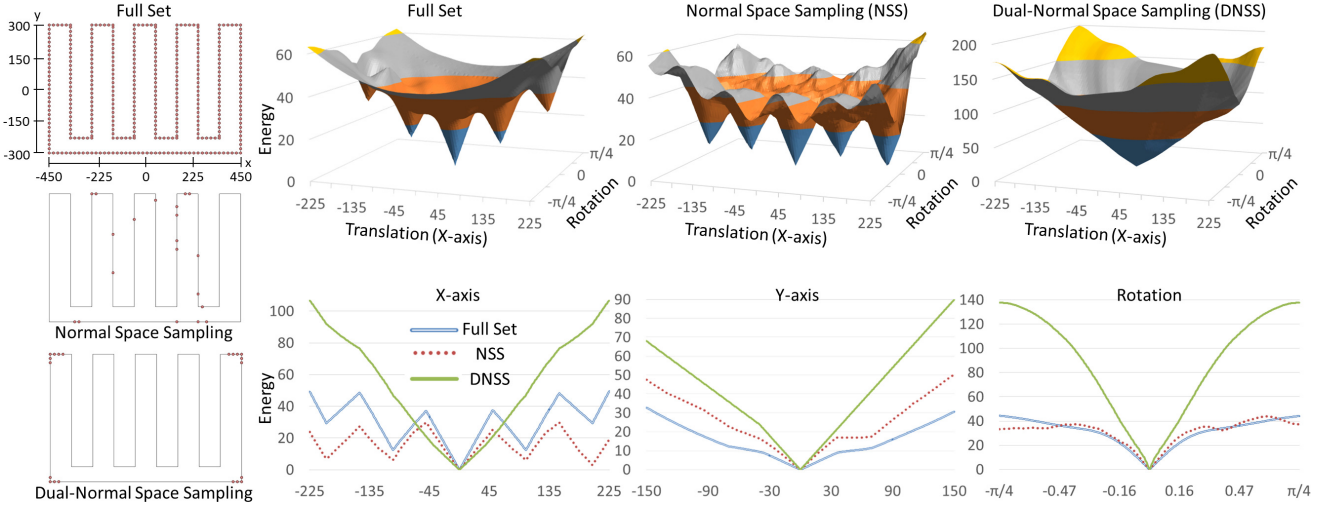


Fig. 1: A 2D teeth shape is used for illustration of the relation between the choice of points and the *range* of convergence in registration. Three different point sets are used: full set, normal space sampling (NSS), and dual-normal space sampling (DNSS). The surface charts in the top row show the energy levels against translation along X -axis and rotation. The three line charts in bottom row show the energy levels against translation in X -axis, Y -axis, and rotation respectively. It is clear that different sets of points give different ranges of convergence. Using the full set of points or the set from NSS has multiple local optima shown in the surface charts, and it is more clear in the line charts that they give the range of convergence ($-50, 50$) along the X -axis. Conversely, the set from DNSS gives only one global optimal as shown in the surface chart as well as the line charts. The success of registration is highly related to the choice of points.

for better strategies to pick points such that the range of convergence is enhanced.

There are different strategies proposed for point selection: uniform sampling, random sampling, normal space sampling [7], curvature sampling [8], sampling on intensity or color, etc. While the feature-based methods [9] normally have a higher robustness, they require addition information like curvature or color. The normal-based approaches are intuitive to understand and straightforward to implement, so they remain the most commonly used point selection algorithm. For example, the *Normal Space Sampling* (NSS) chooses a certain number of points such that the distribution of normals among selected points is as-large-as-possible. The rationale is to sample enough constraints to determine all the components of transformation. However, it can primarily deal with translational components, but not rotational ones. The approach is further extended by covariance sampling [10], [11] that performs stability analysis to select geometrically stable points that can bind the rotational components as well. The method bases on kinematics to find six orthogonal axes and immobilizes the object in those axes, which is promising but not always robust. This is because the initial position is arbitrary and may not fall into one of the axes, so the covariance sampling may not be able to account for all translations and rotations. Following the idea, this paper affirms the importance of binding the rotational components and finds that the selected points constrains the rotational space very differently from the translational, due to the special structure of $SO(3)$. There are even points that always diverge the results in the rotational space. A novel point selection method called Dual-Normal Space Sampling (DNSS) is developed to

sample points carefully, such that both the translational and rotational components are properly constrained. The contributions of this paper are summarized as follows:

- 1) This study analyzes convergence and theoretically shows that points can have a negative return from a rotation, so the convergence is highly related to the selection of points.
- 2) The rotational convergence is derived as a quantitative measure of how a point constrains the rotational components, and it is used to determine the selection of points.
- 3) A uniform sampling in dual-normal space is developed to determine all the translational and rotational components, and its computational complexity is close to NSS.

The developed dual-space space sampling (DNSS) is simple, neat, and effective. Surprisingly, experimental results show that DNSS as a normal-based method can even outperform the feature-based methods in terms of robustness. There is an example showing that DNSS can achieve convergence from an orthogonal initial position while no other methods can achieve. As a result, DNSS is reliable and promising as it can widen the range of convergence without the need of identifying features or additional information.

The rest of the paper is structured as follows. Section II briefs the related works, and Section III analyzes the convergence for translational and rotational components. After that, the details of dual-normal space sampling are given in Section IV. Experimental results and analyses are presented in Section V, and the paper is concluded in Section VI.

II. RELATED WORKS

Registration is a very popular research topic due to its numerous applications, and there are too many related works to be included here. Interested readers are referred to some survey papers [12]–[14]. This section mainly reviews the works related to ICP and the point selection methods.

A. Registration methods

When the inputs have arbitrary positions and orientations, global registration methods are used to find a rigid transformation to roughly align the inputs. Some popular global alignment methods, e.g., 4PCS [15], [16], use RANSAC method to find a set of candidate correspondences from two datasets and choose the best alignment. When the inputs are initialized closely to each other, fine registration is done to refine the alignment. Iterative Closest Point (ICP) and its variants [7] are widely used and there are many applications relying on ICP for fine registration. Recently, there are a number of globally optimal methods [17], [18] proposed to combine both global and fine registration based on the branch-and-bound (BnB) framework. The BnB optimization for registration has a theoretical optimality guarantee, but it is usually time-consuming. To speed up the optimization, Go-ICP [17] integrates ICP into the BnB scheme as an inner loop. Therefore, ICP takes a very important role in registration problems. Some other methods intend to improve the robustness of ICP by modeling the distribution of the points. For example, Jian et al. [19] modeled each point set using Gaussian mixture models (GMMs) directly to align two distance functions. Myronenko and Song [20] considered the points of the first dataset as the centroids of the GMMs and fitted them to the second dataset as a probability density estimation problem. Horaud et al [21] developed an Expectation Conditional Maximization for Point Registration (ECMPR) algorithm, which is an EM-like algorithm, to handle unknown correspondences via mixture models. These methods are generally computational and memory demanding, and some of them even could not be solved in closed-form.

B. Point selection

The performance of ICP heavily depends on the selection of points because sub-sampling can speed up the algorithm and more importantly the selected points determine the convergence of registration. In fact, there are many different sampling variants appeared in literature. Besides those have been already mentioned in the Introduction, Iterative Closest Normal Point (ICNP) [22] shows that the normals contain more discriminatory information than the coordinates of the points, and directly finds correspondence and alignment by the normals. There are works using different local shape descriptors to select points for registration (see survey [23]); for example, curvature map [24], integral volume descriptor [25], intrinsic wave descriptor [26], polynomial descriptor [27]. Based on the descriptors, the points that have rare descriptor values are selected for registration.

These approaches expect the rare points can uniquely define the transformation between the input datasets. Although using rare points may be a good strategy for registration, not every model has distinguishable features, and it is computationally expensive to compute the descriptors for every point in the datasets.

A similar problem in finding critical points is appeared in the fixture and grasping problem, which immobilizes a workpiece accurately and securely during machining or in robotic applications (see surveys [28], [29]). Most of the works in *Computer-Aided Fixture Design* (CAFD) minimize the number of contacts needed for form closure (four in 2D, and seven in 3D), i.e., seven contacts are used to impede all the degrees of freedom of a workpiece purely based on the geometrical placement. The efforts in this field have resulted in numerous CAFD applications using various methods, such as expert system [30], Case-Based Reasoning (CBR) [31], and Genetic Algorithm (GA) [32], etc. Nevertheless, similar to the problem of covariance sampling, even having only seven points may be sufficient to constrain an object from leaving the current position, it may not be enough to attract an object to the desired position from an arbitrary initial position.

III. CONVERGENCE ANALYSIS

Before discussing the details of dual-normal space sampling, this section first analyzes the convergence and shows the difference between translation and rotation. The derivation will be used as a quantitative measurement in point selection. The convergence is studied by measuring how much a point returns back from a rigid motion in one iteration. In mathematics, rigid motions in 3D Euclidean space \mathbb{R}^3 generate a special Euclidean group denoted $SE(3)$. It has as subgroups the translational group $T(3)$ and the special orthogonal group $SO(3)$ – rotational group. The translational group is presented first, and it is followed by the rotational one. Without loss of generality, the motion is assumed to be small, and thus the surface is flat locally, e.g., the point-to-tangent [33] surface approximation is applied.

A. Translational group

A translation changes the position of an object by moving every point by the same amount in a given direction, and thus an element from the translation group $T(3)$ can be solely described by a vector $\mathbf{v} \in T(3)$. Take Fig. 2(a) as an example, a point \mathbf{p} is translated by \mathbf{v} to a new position $\mathbf{p}' = (\mathbf{p} + \mathbf{v})$. Let the point normal as \mathbf{n} ($\|\mathbf{n}\| = 1$) and the closest point of \mathbf{p}' on the surface is \mathbf{q} , the distance error can be minimized by moving \mathbf{p}' to \mathbf{q} by a translation vector

$$\overrightarrow{\mathbf{p}'\mathbf{q}} = (-\mathbf{v} \cdot \mathbf{n})\mathbf{n}.$$

If \mathbf{p} is the only sample point, $\overrightarrow{\mathbf{p}'\mathbf{q}}$ will minimize the energy to zero, i.e., $d(\mathbf{q}, \mathcal{S}) = 0$. It is not in the optimal position, and more points are needed in practice. Here, the return of the motion is measured by how much it compensates

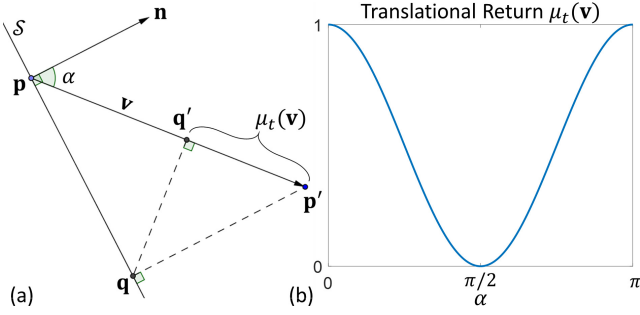


Fig. 2: (a) A point p with normal n is translated by a vector v to p' . The closest point of p' on the surface S is q , and the translational return $\mu_t(v)$ is defined with q' , which is the projected point of q on v . (b) The return $\mu_t(v)$ is plotted against the angle α .

the translation v . Projecting $\overrightarrow{p'q}$ onto the vector v , the translational return is defined as:

$$\mu_t(v) = \frac{\|\overrightarrow{p'q}\|}{\|v\|} = -\frac{(\overrightarrow{p'q} \cdot v)}{\|v\|^2} = \frac{(v \cdot n)^2}{\|v\|^2} = \cos^2 \alpha, \quad (2)$$

where α is the angle between the translation v and the point normal n . It can be seen that $\mu_t(v)$ only depends on the angle α , which is plotted in Fig. 2(b). The return is at its maximum when $\alpha = 0$ or π , i.e., the normal is parallel to the translation.

Remark 1. When the point normal aligns with the translation vector, the translational return is maximized.

If the direction of a translation is known, the best choice is to sample points with normal parallel to that direction, so that the return can be maximized. Nevertheless, when the direction is unknown, points should be picked to account for all possible directions. This is a trade-off strategy as the minimization is done for all the points. If some of the directions have more points than others, the results will be biased and some directions might be omitted. Therefore, a balance way is to select points with normal equally in all directions, so that the return is equalized in the whole normal space. This agrees with the strategy of Normal Space Sampling (NSS) that samples points uniformly across the normal space.

Conjecture 1. An effective sampling is to pick points uniformly to equalize the returns in the normal space.

B. Rotational group

While a translation can be interpreted as shifting the origin of the coordinate system, a rotation is a transformation that preserves the origin. Every non-trivial rotation is determined by its axis of rotation (a line a through the origin o) and its angle of rotation (θ). Therefore, optimizing the rotation parameters by definition is more challenging than the translation parameters, due to the special structure of $SO(3)$.

An element in the translational group $T(3)$ is a vector v , and the translational return can be described by the included

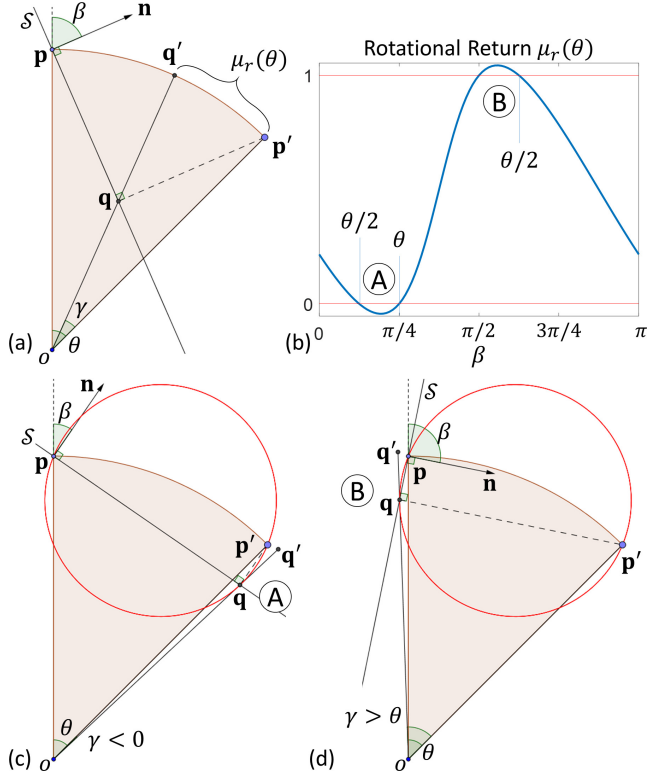


Fig. 3: (a) A point p with normal n is rotated around a center o by an angle θ to p' . The closest point of p' on the surface S is q , and the rotational return $\mu_r(\theta)$ is defined with an angle γ . (b) The rotational return $\mu_r(\theta)$ is plotted against the angle β . Region A visualized in (c) gives a negative return, and region B visualized in (d) gives a return greater than 1.

angle (α) between v and n . In contrast, an element in the rotational group $SO(3)$ is a couple (a, p) , where a is the rotational axis and p is the radius – a center-to-point vector with the origin is the center, i.e., $p \equiv \overrightarrow{op}$. The rotational return is thus related to the three vectors a , p and n . The vectors form a 3D space and the return can be described by two angles. One is the angle β between p and n , and the other one is the angle α between a and $p \times n$ (later named as rotational normal). The angle α here shares the same meaning as the one in the translational return, between the axis of motion and the normal, and its effect to the return is a factor of $\cos^2 \alpha$ as studied in Eq.2. The following discussion mainly focuses on β and assumes $\alpha = 0$, i.e., the motion and its return are on the same rotational plane.

In Fig. 3(a), a point p is transformed to p' in a clockwise direction by a rotational angle (θ) at a rotational center (o) around a rotational axis (a) perpendicular to paper. The closest point of p' on the surface is q , and the optimization is to rotate in an anticlockwise direction to align p' to the point q . Assume the returning angle is γ measured in an opposite direction of θ , the amount of return is the arc length $\|\overrightarrow{p'q'}\| = \|p\|\gamma$, and thus the rotational return

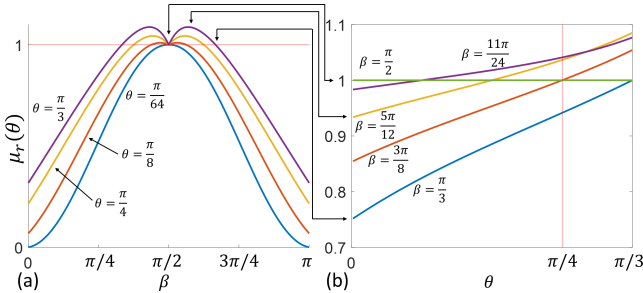


Fig. 4: The rotational return $\mu_r(\theta)$ is plotted against (a) β and (b) θ with different values of the other.

referenced to θ is defined as

$$\mu_r(\theta) = \frac{\|\mathbf{p}\| \gamma}{\theta}. \quad (3)$$

Based on trigonometry and chord, γ is calculated by

$$\gamma = (\theta - \tan^{-1}(\frac{\|\overrightarrow{\mathbf{pq}}\| \sin \beta}{\|\mathbf{p}\| - \|\overrightarrow{\mathbf{pq}}\| \cos \beta})), \quad (4)$$

where

$$\begin{aligned} \|\overrightarrow{\mathbf{pq}}\| &= \|\overrightarrow{\mathbf{pp'}}\| \cos(\beta - \theta/2) \\ \|\overrightarrow{\mathbf{pp'}}\| &= 2\|\mathbf{p}\| \sin(\theta/2). \end{aligned}$$

Therefore, $\mu_r(\theta)$ depends on the rotational radius $\|\mathbf{p}\|$, the rotational angle θ , and the angle β between the normal \mathbf{n} and \mathbf{p} , i.e., $\mu_r(\theta) = f_r(\|\mathbf{p}\|, \theta, \beta)$. In Fig. 3(b), $\mu_r(\theta)$ is plotted against β for $\|\mathbf{p}\| = 1$ and $\theta = \pi/4$. Unlike the translational return that always falls in the range of $[0, 1]$, the rotational return can be less than 0 (indicated as A) or greater than 1 (indicated as B), where zone A is $\beta = (\theta/2, \theta)$ and zone B is $\beta = (\pi/2, (\pi + \theta)/2)$. This phenomenon is demonstrated in Fig. 3(c) and (d), where the circle is the locus of the closest point \mathbf{q} according to different values of β . The figure shows that there are two parts of the circle out of the spectral angle between \mathbf{p} and \mathbf{p}' ($\equiv \overrightarrow{\mathbf{op'}}$). One is beyond \mathbf{p}' resulting $\gamma < 0$, the other one is behind \mathbf{p} resulting $\gamma > \theta$. It is a critical difference between translation and rotation. If the return is negative $\mu_r(\theta) < 0$, the optimization fails to return from the induced rotation θ and will never be able to align the datasets unless they are already aligned, i.e., $\theta = 0$.

Observation 1. *The rotational component can be diverged even the registration energy is decreasing.*

Based on the observation, this research makes the following hypothesis.

Hypothesis 1. *Sampling points for both the translational and the rotational components gives better convergence to registration than only for the translational one.*

In terms of point selection, it is desired to pick the points with the return close to or even greater than 1, but certainly not to pick points that give negative returns. Therefore, $\mu_r(\theta) = f_r(\|\mathbf{p}\|, \theta, \beta)$ can be utilized to guide the selection of points for registration, where $\|\mathbf{p}\|$ is the point-to-center distance that is well-defined with the center, e.g., the mass

center, and β is the angle between \mathbf{p} and the normal \mathbf{n} . The angle θ stands for the angle difference between the two datasets around a rotational axis, which can be used to control the sensitivity of registration. It is desired to set θ as large as possible, so that the registration can work for a larger range of initial positions and orientations. Figure 3(b) shows the return for the clockwise rotational motion, and it is similar for the anticlockwise motion, which is a mirror copy of the clockwise one. By considering both directions at the same time, zone A in one direction and zone B in the other one will touch each other when $\pi/2 - \theta/2 = \theta$, i.e., $\theta = \pi/3$. Therefore, the maximum value of θ that can be chosen without doing any harm to other direction is $\pi/3$.

During the optimization, the angle difference θ between datasets is expected to be decreasing, from *far* to *close*. Therefore, the contribution of each point to the rotational return $\mu_r(\theta)$ is changing throughout the registration. Figure 4(a) shows the mirrored rotational return against the angle β between \mathbf{p} and \mathbf{n} , and the maximum value is taken, i.e.,

$$\mu_r(\theta) = \max(f_r(\|\mathbf{p}\|, \theta, \beta), f_r(\|\mathbf{p}\|, \theta, -\beta)). \quad (5)$$

It is plotted with different values of θ (from $\pi/64$ to $\pi/3$) to illustrate different stages during registration. Correspondingly, the returns against the angle θ with different values of β are plotted in Fig. 4(b). It can be seen from the figures that when $\beta = \pi/2$, the return is always 1, otherwise the return is varying from less than 1 to greater than 1, such as the case of $\beta = 5\pi/12$. It is good that the return is always 1, but it is even better that the return is greater than 1 to achieve higher convergence. However, there is a trade-off in the convergence between the far-mode and the near-mode. Takes $\beta = \pi/3$ in Fig. 4(b) as an example, its return is 1 when $\theta = \pi/3$ but degrades to ~ 0.75 when $\theta = 0$. It is not comparable to $\beta = \pi/2$ that always gives a return of 1, and thus $\mu_r(\theta)$ should have a smaller value for $\beta = \pi/3$ than $\beta = \pi/2$, where setting $\theta = \pi/3$ is obviously not a good choice as it gives a same value to both cases. To balance both far and near modes, the ideal case is that the return is greater than 1 when the datasets are far away and close to 1 when the datasets are close. In this paper, $\theta = \pi/4$ is selected for point selection.

Next section will present the details of the point selection method considering the rotational component.

IV. DUAL-NORMAL SPACE SAMPLING

The above discussion gives the Observation 1 that the rotational component can be diverged and makes the Hypothesis 1 that the points should be selected for both translational and rotational components. Unfortunately, the widely used NSS method only considers the translational component as discussed in Section III-A, and feature-based methods locating rare points generally do not follow Conjecture 1 to balance the convergences in different directions. To test the hypothesis, this section presents a new point selection method to sample points uniformly in a dual-normal space, which includes both translational and

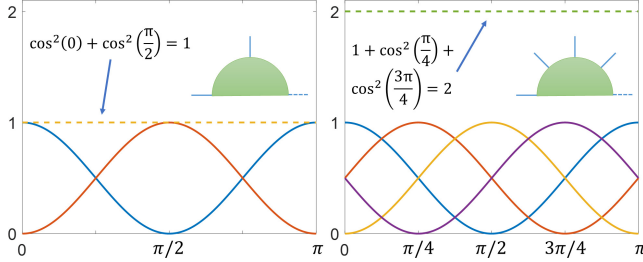


Fig. 5: Point contribution and equalized return among the normal space in 2D.

rotational components. Before that, the strategy used in NSS is revisited to demonstrate the underlying axiom of uniform sampling.

A. Equalizing returns among normal space

Figure 2 has shown how a point contributes to the translational return in different directions with respect to the angle α between normal and translational vector. The total return in a direction can be calculated by summing up the contributions from all selected points to that direction. Due to the translational return in Eq.(2) is a cosine-squared function, if uniform sampling is used, the total returns can be equalized among all directions. The value of the equalized return is calculated as

$$\bar{\mu} = \sum_{i=0}^{n-1} \cos^2(i \times \frac{\pi}{n}) = \frac{n}{2},$$

where n is the number of sampling points. For example, if points are selected by a separation of $\frac{\pi}{2}$ in terms of their normal, the total return for any direction will be equal to 1 as shown in Fig. 5(left). In other words, uniform sampling can equalize the returns among normal space and Eq.(2) needs not to be computed explicitly, i.e., it only needs to count the number of points selected in each sampling direction.

Remark 2. As long as the sampling is uniform, Conjecture 1 is satisfied implicitly and the angle α can be ignored.

On the other hand, the value $\bar{\mu}$ can be increased by increasing the sample size. One example of selecting points by a separation of $\frac{\pi}{4}$ in normal is shown in Fig. 5(right), in which $n = 4$ and the total return is increased to 2.

Normal is a unit vector, so uniform sampling in the normal space is equivalent to sampling points uniformly on a unit sphere. To sample points on the surface of a unit sphere, the 2D spherical coordinates (θ, ϕ) from mathematics can be used instead of the 3D Cartesian coordinates (x, y, z) , where θ is the azimuthal angle in the xy -plane from the x -axis with $0 \leq \theta < 2\pi$ and ϕ is the polar angle from the positive z -axis with $0 \leq \phi \leq \pi$. Since the area element (solid angle) $dA = (\sin \phi) d\theta d\phi = -d\theta d(\cos \phi)$ is a function of θ and $\cos \phi$, the spherical coordinates are selected from uniform distributions $\theta \in [0, 2\pi)$ and $\phi = \cos^{-1}(2u - 1)$ with $u \in [0, 1]$. All the points of the dataset are bucketed according to the position of

the normals using the spherical coordinates. For a normal position (x, y, z) , its spherical coordinates can be computed by $\phi = 2\pi z$ and using the trigonometric ratios in the four quadrants with the values of x and y for θ . After that, point selection is done by sampling uniformly across the buckets, and a point is randomly picked in a bucket that contains multiple points.

B. Equalizing returns among dual-normal space

Uniformly sampling in normal space constrains the translational component well, but Observation 1 finds that sampling for the rotational component is critical to prevent divergence. This paper defines a dual-normal space to enable the sampling for rotational component. For a small motion, cross product can be used to describe the infinitesimal generators of rotation, and the motion can be expressed linearly as

$$(\mathbf{r} \times \mathbf{p} + \mathbf{t}) \cdot \mathbf{n} = [\begin{array}{cc} \mathbf{t} & \mathbf{r} \end{array}] \left[\begin{array}{c} \mathbf{n} \\ \mathbf{p} \times \mathbf{n} \end{array} \right].$$

It can be seen that the translational component \mathbf{t} is corresponding to the normal \mathbf{n} and the rotational component \mathbf{r} is corresponding to $(\mathbf{p} \times \mathbf{n})$. Because of these correspondences, here gives the new definitions of normal with respect to translation and rotation.

- Translational normal (t-normal): \mathbf{n}
- Rotational normal (r-normal): $\mathbf{p} \times \mathbf{n}$

The dual-normal space is the combination of t-normal and r-normal spaces. Following the Conjecture 1, the ideal sampling is to equally pick points among the normal spaces. Under the new definition of normal spaces, the sampling should be done in both the t-normal and r-normal spaces, and the returns should be equalized on both spaces too. The cross product $\mathbf{p} \times \mathbf{n}$ is a vector, so the sampling in the r-normal space is the same as that in the t-normal space by bucketing the points using the 2D spherical coordinates.

As mentioned in Remark 2, uniform sampling for translational return is as simple as counting the number of points in each bucket. However, the rotational return in Eq.(3) also depends on the angle β and the radius $\|\mathbf{p}\|$, which means that the contribution of can be different point-by-point and the sampling must take each one into account to make sure the total return can be equalized. Moreover, the t-normal and r-normal spaces are actually interrelated, i.e., one sample point contributes to both spaces. It is therefore an optimization problem to equalize the returns in both spaces at the same time. In this paper, a greedy algorithm is developed that always picks a point with the largest value of rotational return from the least constrained bucket sequentially. Specifically, the points in each bucket are sorted by the value computed using Eq.(5) in descending order. Each bucket is also associated with a constraint value, which will be increased whenever a point in the bucket is picked, and the value is used to record the contributions of the selected points. The buckets are sorted in ascending order by the constraint values, and each time a point is picked from the first bucket. Both the sorting of points and

Algorithm 1 Dual-Normal Space Sampling

Input: Point cloud P , target number of samples N
Output: Sampling points M

```

//initialize heaps for points in each bucket
{ $b_t$ } ← buckets all points in  $P$  by t-normal  $\mathbf{n}$ 
{ $b_r$ } ← buckets all points in  $P$  by r-normal  $\mathbf{p} \times \mathbf{n}$ 
for all buckets  $b \in \{b_t, b_r\}$  do
     $b.heap \leftarrow$  create max heap for points  $p \in b$  with  $p.\mu$ 
    from Eq.(5) as key

//initialize heap for buckets
for all buckets  $b \in \{b_r\}$  do
     $PickPoint(b)$  //see below
     $BHeap \leftarrow$  create min heap for buckets  $\forall b \in \{b_t, b_r\}$ 
    with constraint  $b.constraint$  as key

//main sampling process
while  $M.size() < N$  do
     $b \leftarrow BHeap.GetTop()$ 
     $(b_t, b_r) \leftarrow PickPoint(b)$ 
     $BHeap.Update(b_t, b_r)$ 

Function  $PickPoint(\text{Bucket } b)$ 
     $p \leftarrow b.heap.GetTop()$ , add  $p$  to  $M$ 
     $(b_t, b_r) \leftarrow$  Get the buckets where  $p$  locates
     $b_t.heap.Remove(p)$ ,  $b_t.constraint += 1$ 
     $b_r.heap.Remove(p)$ ,  $b_r.constraint += p.\mu$ 
    return  $(b_t, b_r)$ 

```

buckets are implemented by a heap data structure, and the pseudo-code of the dual-normal space sampling is given in Algorithm 1. Before any points are picked, the constraint values of all buckets are zero, which is not meaningful to create a heap. Therefore, an optional initialization step can be performed to select a point from each of the buckets in the r-normal space.

C. Relationship between translational and rotational return

One may notice that the rotational return depends on the size of model due to the term $\|\mathbf{p}\|$, and thus the values for translation and rotation are actually in different scales. Due to ICP itself is a geometric problem, it is not reasonable that the size of model affects the importance between translation and rotation, and it can be easily verified that ICP is scale-independent. For instance, running ICP on a model and its scaled-down version (e.g., 10^{-4} times smaller) will give identical results. Therefore, the relationship between the translational and rotational return should be understood and properly normalized, and this section will test and evaluate the performances of different normalization methods, from which the best one is used.

The rotational return or the r-normal space should be normalized with respect to the object's size, i.e.,

$$\begin{bmatrix} \mathbf{n} \\ \frac{1}{L}\mathbf{p} \times \mathbf{n} \end{bmatrix} \in \Re^6, \quad (6)$$

where L is the normalization factor. The problem is how to set L to give a correct normalization. The most common

		Skull	Airplane	Vase	R-Arm
1	I	377	132	146	139
	II	×	145	157	146
	III	583	148	168	150
L_{avg}	I	338	132	146	152
	II	×	145	161	161
	III	374	148	171	172
L_{pn}	I	169	159	93	120
	II	394	×	122	×
	III	×	167	×	146
L_{max}	I	310	160	137	152
	II	317	172	154	161
	III	351	191	165	172

TABLE I: Comparison of the normalization methods.

practices [34] is to set $L = L_{avg}$ as the average distance of the points from the center, but there are also other practices such as setting $L = L_{max}$ as the maximum distance (i.e., scale the object to be inscribed in a unit ball) or $L = L_{pn} = \|\mathbf{p} \times \mathbf{n}\|$ to normalize the effect on each point. When normalization is large, e.g., $L = L_{max}$, the constraints to r-normal space are reduced and more points are picked from the buckets in r-normal space. Reciprocally, when normalization is small, e.g. $L = 1$, more points are picked from the buckets in t-normal space. When the normalization is not optimal, the selection of points from the buckets in t-normal and r-normal space is not balanced. Although unbalanced point selection may give better convergence in some cases, it is unstable. In this paper, an experiment is conducted to test and find the best one for ICP. Four normalization methods are tested, including 1, L_{avg} , L_{pn} , and L_{max} , where 1 stands for no normalization. The results are recorded by the number of iteration until ICP is converged. The experiment is done by testing different cases of artificial misalignment (I, II, II) by a translation and a rotation. The setting of the levels are:

- I : $d_x = d_y = d_z = 0.1b$, $\theta = \phi = -10^\circ$
- II : $d_x = d_y = d_z = 0.3b$, $\theta = \phi = 30^\circ$
- III: $d_x = d_y = d_z = -0.5b$, $\theta = \phi = 45^\circ$

where d_x , d_y , d_z relate to the size of model, i.e., b is the radius of circumscribed sphere of the model, and θ and ϕ are the polar and azimuthal angles in spherical coordinates. The sizes of all the testing models are in the scale of 100, and 100 sample points are used in all of the tests. The results of this experiment are shown in Table I. From the table, there are a few observations:

- 1) $L = 1$ and L_{avg} have very similar performance, and they even fail at the same time.
- 2) L_{pn} mostly has the best performance, e.g., for case I on the Vase model, it takes only 93 iterations to converge, while others take at least 137.
- 3) L_{pn} has the most number of failures, i.e., one per example, making it the most unstable one.
- 4) L_{max} does not have a big difference compared to $L = 1$ or L_{avg} , but succeeds in all tests.

Since both $L = 1$ and L_{avg} result in higher constraints in r-normal space and more points are picked from the buckets in t-normal space, their performances are similar (Observation 1), meaning that L_{avg} is as small as $L = 1$ in

terms of normalization. L_{pn} is the most tricky one. On one hand, it is very attractive as it gives the best performance in terms of convergence (Observation 2). On other hand, it gives the worst performance in terms of stability (Observation 3). This is because when the contributions of points disrespect to their distance to rotational center, the points selected are not balanced among the normal spaces, and thus L_{pn} is more sensitive in some directions but it is worse or even fails in some others. Among them, although L_{max} does not always have the best convergence, it is the most stable one (Observation 4). For the sake of generalization, the most appropriate choice for ICP is found to be L_{max} as the normalization factor.

V. EXPERIMENTAL RESULTS

The proposed method is implemented in C++ and tested on a standard PC with an Intel i5 3.2 GHz CPU. In the experiments, mesh surfaces represent the static scene (\mathcal{S}), point clouds represent the moving model (\mathcal{M}), and the highlighted points are the selected points for registration. Noted that the mesh surfaces are used for better visualization purpose only, but the registration is done based on points. The main focus here is to compare the convergence and robustness of different sampling methods. They are tested by different ranges of applied translations (d_x, d_y, d_z) and rotations (θ, ϕ). The results are compared by whether the registration can successfully converge and the number of iterations # taken until ICP converges, where the termination condition is set as the alignment error being smaller than $1e - 5$.

To compare and relate the quality of sampling and performance, a heightmap is used to visualize the constraints of the selected points in each bucket. In this paper, the bucket size is set as $\pi/6$. As the 2D spherical coordinates are $0 \leq \theta < 2\pi$ and $0 \leq \phi \leq \pi$, there are 12×6 buckets for the t-normal space. Due to the reason that the rotational return needs to be maximized in one direction without doing any harm to the other direction, both directions in the rotation are considered together as shown in Eq.(5). Therefore, the same vectors with different signs are grouped together, and there are 6×6 buckets for the r-normal space. The heightmaps are rendered as a 12×6 and 6×6 grayscale images respectively, with black representing minimum constraints and white representing maximum constraints. The quantitative measures in terms of the mean constraints μ and the percentage of empty buckets \emptyset are also listed together with the heightmaps, where both of them are highly related to the convergence. The mean μ is the expected return in one ICP iteration and the empty ratio \emptyset reflects how many different directions can be covered. When the ratio \emptyset is low, the registration process may oscillate jumping back and forth in the $SE(3)$ space to find a right way to converge. This results in a poor convergence, especially when the datasets are far away from each other (in the far-mode). On the other hand, the mean μ affects the speed of convergence which is significant near a minimum, i.e., in the near-mode. It is desired that the mean

μ is high and the empty ratio \emptyset is low. In the following, the proposed DNSS method will be compared with the normal-based methods first and then the feature-based methods.

A. Comparison with normal-based methods

To test the Hypothesis 1 that proposes sampling points uniformly across both the t-normal and r-normal spaces gives better performance, a number of experiments are done to compare the convergence between DNSS and other normal-based methods. The normal-based methods sample the input point cloud by normal directions requiring only the normal information. The Normal-Space Sampling (NSS) [7] and Covariance Sampling (CovS) [10], [11] are two representatives, where NSS samples uniformly across the angular space according to the position of the normals and CovS picks points not to form a kinematic surface.

One comparison in 2D case is shown in Fig. 1, where a teeth shape with repeated features along the X -axis is used. The figure shows that NSS and Full Set have very similar performances in terms of the energy patterns shown in the bottom row by translations along the X -axis and Y -axis as well as the rotation. From the combined translation and rotation charts shown in the top row, although Full Set has a smoother pattern, they have the same number of local minimums and the same range of convergence. Therefore, NSS as a subset is a good representative for the Full Set to speed up the registration process, which makes it the most commonly used sampling method for ICP. However, using all points generally does not give the best performance, and it can be seen that there are multiple minimums along the X -axis due to the repeated tooth features. In contrast, the proposed DNSS selects points around the corners so that it is not affected by the repeated features and gives only one optimum, which can be seen more clearly from the chart of combined translation and rotation (top row). Although DNSS has a slightly lower energy (i.e., slower convergence) in the range of $[-45, 45]$ along the X -axis, the enhanced range of convergence $[-225, 225]$ is more beneficial. Besides, its energies along the Y -axis and in the rotation are significantly higher, resulting in a better convergence overall.

The comparisons with NSS and CovS on 3D models are shown in Fig. 6, and three models (cup, ant, shoe) with different initial positions are tested. This experiment aims to compare the convergence of the methods, so the same number of sample points is used and the initial positions are picked such that all methods can converge. The robustness will be tested in the next section with the feature-based methods together. NSS uniformly samples points among the t-normal space and CovS picks points by the constraints that a point can contribute, so they have quite different characteristics. Generally speaking, NSS has a lower percentage of empty buckets \emptyset and CovS has a higher mean constraint μ . Recalled that the mean μ and the empty ratio \emptyset affect the convergence in the far-mode and the near-mode respectively. Therefore, it can be seen from the examples that NSS converges faster than CovS

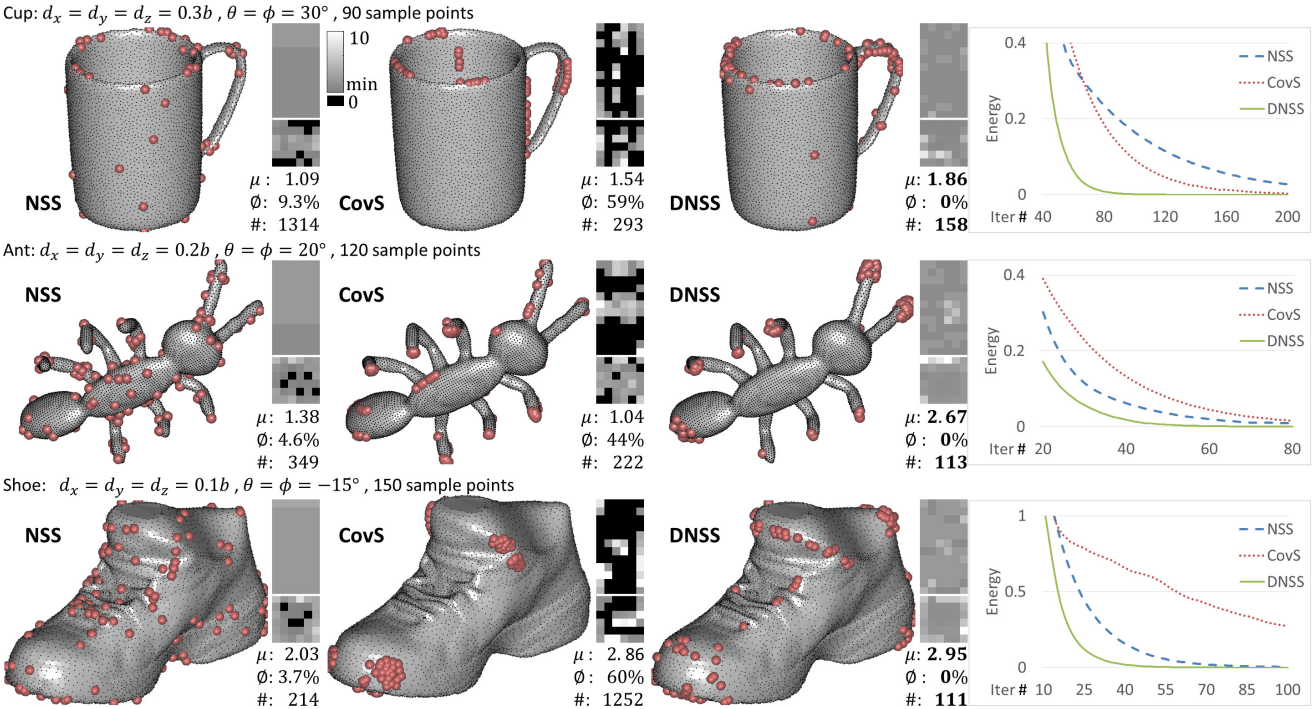


Fig. 6: Comparisons with the normal-based methods: Normal-Space Sampling (NSS) and Covariance Sampling (CovS). Each result is associated with a 12×6 and a 6×6 heightmaps visualizing the constraints in t-normal and r-normal spaces respectively, where μ is the mean constraints, \emptyset is the percentage of empty buckets, and $\#$ is the number of iterations for ICP to converge. The initial positions are given by the applied translations and rotations, where d_x, d_y, d_z are related to the size of the model, i.e., b is the radius of the circumscribed sphere of the model, and θ is the polar angle and ϕ is the azimuthal angle in spherical coordinates.

	Cup	Ant	Shoe	Rabbit	Skull	Airplane	Vase	Rocker arm
$(d_{x,y,z}, \theta \& \phi)$	$0.4b, 10^\circ$	$-0.5b, 20^\circ$	$0.3b, -15^\circ$	$-0.3b, -30^\circ$	$0.1b, 20^\circ$	$-0.2b, 45^\circ$	$0.4b, -50^\circ$	$0.5b, 90^\circ$
sample points	75	75	60	57	51	41	76	75
3D-Harris [35]	315	\times	772	233	\times	518	\times	\times
3D-SIFT [36]	254	157	164	291	320	\times	\times	\times
Mesh Saliency [37]	192	\times	210	208	\times	199	167	\times
Salient pt [38]	161	\times	233	\times	\times	194	145	\times
SD Corner [39]	699	144	284	371	446	\times	201	\times
NSS [7]	808	247	232	284	401	\times	\times	\times
CovS [10]	774	\times	2766	\times	\times	589	\times	\times
DNSS	150	117	182	206	259	152	241	201

TABLE II: Convergence comparison with the point sampling methods by the number of iterations to converge.

in the early iterations, but CovS catches up from behind and reaches the termination condition earlier. For instance, CovS takes #293 and #292 iterations to converge in the cup and ant models, while NSS takes #1314 and #349 iterations respectively. Especially for the cup model that does not have many features, although NSS performs better before iteration #65, it converges slowly at the end due to its low mean constraint μ . However, the success of CovS depends on the initial position in the far-mode because its sampling is not uniform among the normal spaces. If the initial position does not favor the sampling, e.g., in the shoe model, it even takes more than #90 iterations to get the energy down to 0.3, resulting in a total of #1252 iterations to converge. In contrast, DNSS samples points

among all the buckets in both t-normal and r-normal spaces by their returns, so DNSS has no empty buckets and has the highest value of μ in all the models. Living up to expectations, DNSS has the best performance in the tested models taking only #110 ~ 160 iterations to converge. DNSS outperforms NSS and CovS in both far and near modes, which supports the Hypothesis 1.

B. Comparison with feature-based methods

To test the robustness of the proposed DNSS, it is compared with the feature-based methods. Feature-based methods take additional information of mesh surface like curvature, topology, connectivity, and/or color to select

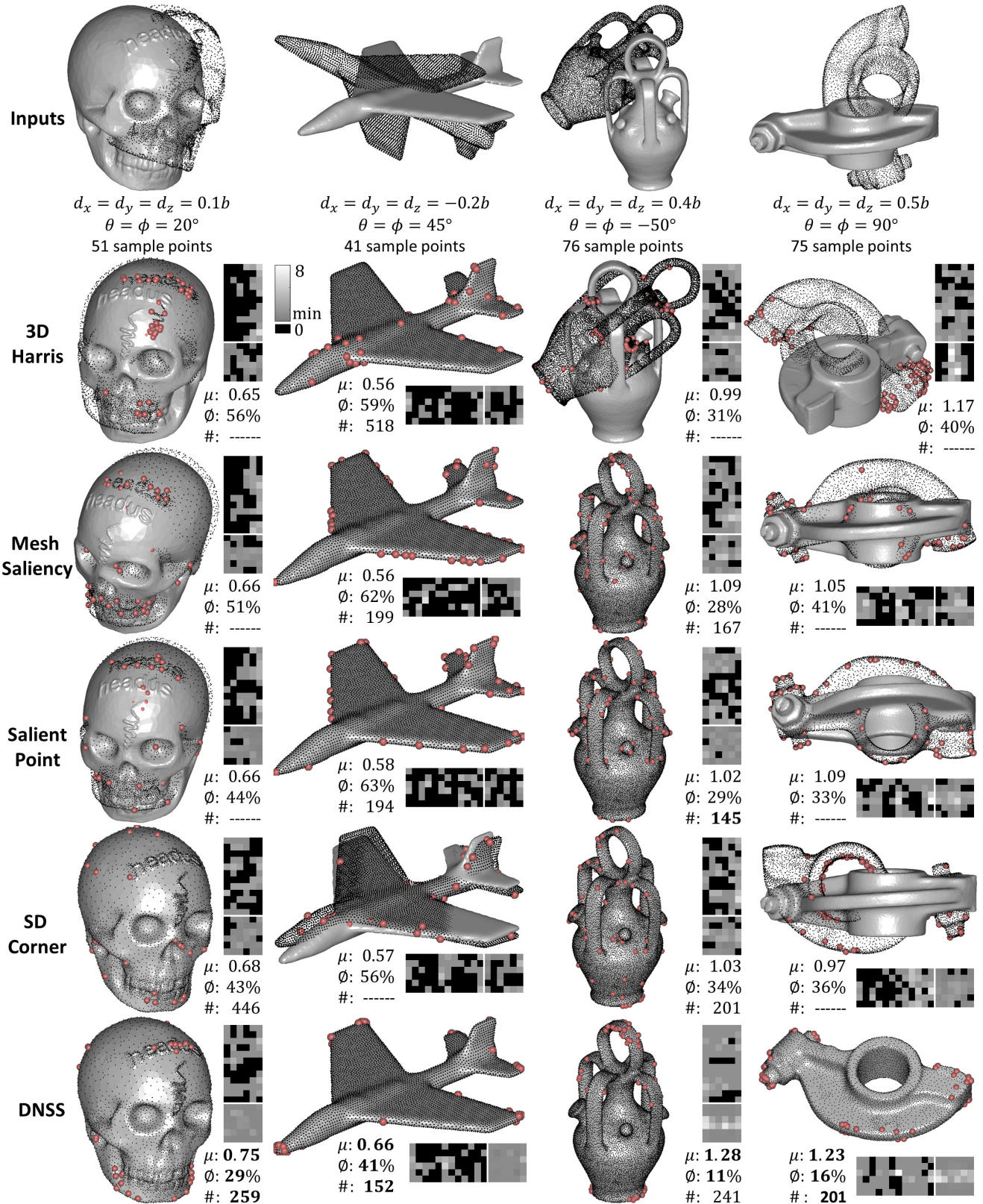


Fig. 7: Comparison with the feature-based methods. The top row shows the input model \mathcal{M} (visualized by point cloud) and scene \mathcal{S} (visualized by surface), and their initial positions by translations (d_x, d_y, d_z) and rotations (θ, ϕ). The registration results of different methods are shown in the following rows, each of which is associated with the heightmaps, the mean constraints μ , the empty ratio \emptyset , and the number of iterations # for ICP to converge.

rare points for registration, and they normally have a higher robustness compared with the normal-based methods [9]. The evaluated methods include 3D-Harris [35], 3D Scale-Invariant Feature Transform (3D-SIFT) [36], mesh saliency [37], salient points [38], and Scale-Dependent (SD) corners [39]. Together with the normal-based methods, they are tested with different models with various shapes, features, and initial positions. The convergence comparison is summarized by the number of iterations taken to converge in Table II, and some selected results are shown in Fig. 7. Due to the rich content of the rare points, feature-based methods generally require few sample points. To have a fair comparison, these experiments use some smaller numbers of sample points ($40 \sim 80$). Noted that it may not be enough for the NSS and DNSS methods to pick at least one point from each of the buckets, but it is actually good to test the robustness of the methods.

Different initial positions are applied to test the limit of each method and they are designed in different challenging levels, i.e., the translations are ranging from $\pm 0.1b$ to $\pm 0.5b$ where b is the radius of circumscribed sphere of the model, and the rotations are ranging from 10° to 90° (see Table II). Generally, the success of registration for a model of translational symmetry is prone to translations and for a model of axial symmetry is prone to rotations. For example, the cup model is axially near-symmetry, so all the methods are quite successful due to small rotations of 10° , even translations of $0.4b$ are large. A similar situation is also found in the shoe model, where all methods succeed with the initial position of $(0.3b, -15^\circ)$. On the other hand, as the ant model is translational near-symmetry, large translations of $-0.5b$ make most of the methods failed. Only 3D-SIFT, SD Corner, NSS, and DNSS are successful in this example, and DNSS has the best convergence (#117). Figure 7 shows some more challenging test cases in terms of model geometry and initial positions, where only $3 \sim 4$ methods can converge in these examples. A skull model has a spherical shape, and even it has some features on the surface, registration can be easily trapped in local minimums in the $SO(3)$ space. Large transformations are applied to an airplane model $(-0.2b, 45^\circ)$ and a vase model $(0.4b, -50^\circ)$. The most challenging example is in a rocker arm model, where the highest level of translations and rotations $(0.5b, 90^\circ)$ is applied. The initial position can be seen in Fig. 7 that the model \mathcal{M} and the scene \mathcal{S} are basically perpendicular to each other. None of the methods except DNSS can succeed in this example, and the steps in registration for the rocker arm model using DNSS are demonstrated in Fig. 8. In summary, besides DNSS, all methods work well on some models, but fail in the others. Among which, SD Corner has the best robustness and fails only in the airplane and rocker arm models. Surprisingly, DNSS is successful in all the test cases and it has the best convergence, except in the shoe and vase models DNSS is slightly slower. This is because the feature-based methods may work particularly well in certain initial positions, but DNSS has a good balance between convergence and robustness. Therefore, DNSS is promising for registration

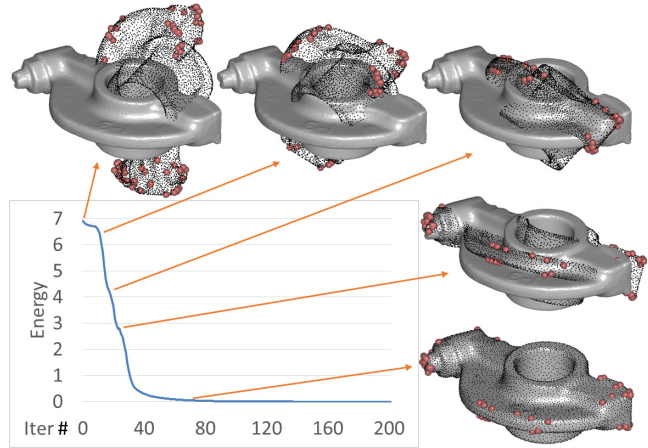


Fig. 8: Registration detail for rocker arm using DNSS.

applications, and it also supports the Conjecture 1 that uniform sampling is an effective way for point selection.

VI. CONCLUSION

This paper presents a novel point selection for 3D ICP registration. This method is based on the observation of the structural difference between the translational group and the special orthogonal group, and the hypothesis proposes that the point selection should take the difference into account. Therefore, this paper gives a new definition to the normal space and separates it to a translational normal and a rotational normal. Quantitative measurements are derived to calculate the contributions of each point for the new normal spaces. A Dual-Normal Space Sampling (DNSS) is then developed to sample points uniformly across the two normal spaces, such that the constraints provided by the sampled points are equalized among the spaces. The computational cost of DNSS is similar to that of the normal-based methods, and the experimental results show that the proposed method is superior to both the normal-based and feature-based sampling methods. DNSS can even succeed in an orthogonal initial position where no other methods can, which supports the hypothesis.

As a variant of ICP under the category of point selection, DNSS extends the range of convergence and has less demand on the initial position. It is a very good complementary to most of the recently developed registration methods that guarantee global optimum, as well as other ICP variants such as anisotropic ICP [40] and sparse ICP [41] to deal with outliers and noises.

ACKNOWLEDGMENT

I acknowledge the support of the Natural Sciences and Engineering Research Council of Canada (NSERC) [RGPIN-2017-06707].

REFERENCES

- [1] Y. Lee, J. Chen, C. W. Tseng, and S.-H. Lai, “Accurate and robust face recognition from RGB-D images with a deep learning approach,” in the *BMVC*, York, UK, Sept 2016.

- [2] A. Segal, D. Haehnel, and S. Thrun, "Generalized-ICP," in *Proceedings of Robotics: Science and Systems*, Seattle, USA, June 2009.
- [3] A. Geiger, P. Lenz, and R. Urtasun, "Are we ready for autonomous driving? the kitti vision benchmark suite," in *IEEE CVPR*, June 2012, pp. 3354–3361.
- [4] F. Donoso, K. Austin, and P. McAree, "How do ICP variants perform when used for scan matching terrain point clouds?" *Robotics and Autonomous Systems*, vol. 87, pp. 147 – 161, 2017.
- [5] H. Pottmann, Q.-X. Huang, Y.-L. Yang, and S.-M. Hu, "Geometry and convergence analysis of algorithms for registration of 3D shapes," *International Journal of Computer Vision*, vol. 67, no. 3, pp. 277–296, 2006.
- [6] P. J. Besl and N. D. McKay, "A method for registration of 3-D shapes," *IEEE Trans. Pattern Anal. Mach. Intell.*, vol. 14, no. 2, pp. 239–256, Feb. 1992.
- [7] S. Rusinkiewicz and M. Levoy, "Efficient variants of the ICP algorithm," in *International Conference on 3DIM*, Jun. 2001.
- [8] E. Rodol, A. Albarelli, D. Cremers, and A. Torsello, "A simple and effective relevance-based point sampling for 3D shapes," *Pattern Recognition Letters*, vol. 59, pp. 41 – 47, 2015.
- [9] Y. Zhao, Y. Liu, and Z. Zeng, *Using Region-Based Saliency for 3D Interest Points Detection*. Berlin, Heidelberg: Springer Berlin Heidelberg, 2013, pp. 108–116.
- [10] N. Gelfand, L. Ikemoto, S. Rusinkiewicz, and M. Levoy, "Geometrically stable sampling for the ICP algorithm," in *Proceedings of International Conference on 3DIM*, Oct 2003, pp. 260–267.
- [11] T.-H. Kwok and K. Tang, "Improvements to the iterative closest point algorithm for shape registration in manufacturing," *ASME. J. Manuf. Sci. Eng.*, vol. 138, no. 1, p. 011014, 2015.
- [12] J. Salvi, C. Matabosch, D. Fofi, and J. Forest, "A review of recent range image registration methods with accuracy evaluation," *Image Vision Comput.*, vol. 25, no. 5, pp. 578–596, May 2007.
- [13] O. van Kaick, H. Zhang, G. Hamarneh, and D. Cohen-Or, "A survey on shape correspondence," *Computer Graphics Forum*, vol. 30, no. 6, pp. 1681–1707, 2011.
- [14] G. K. Tam, Z.-Q. Cheng, Y.-K. Lai, F. Langbein, Y. Liu, A. D. Marshall, R. Martin, X. Sun, and P. Rosin, "Registration of 3D point clouds and meshes: A survey from rigid to nonrigid," *IEEE Trans. Vis. Comput. Graphics.*, vol. 19, no. 7, pp. 1199–1217, 2013.
- [15] N. Mellado, D. Aiger, and N. J. Mitra, "Super 4PCS fast global pointcloud registration via smart indexing," *Comput. Graph. Forum*, vol. 33, no. 5, pp. 205–215, 2014.
- [16] J. Huang, T. H. Kwok, and C. Zhou, "V4PCS: Volumetric 4pcs algorithm for global registration," *ASME. J. Mech. Des.*, vol. 139, no. 11, pp. 111403–9, 2017.
- [17] J. Yang, H. Li, D. Campbell, and Y. Jia, "Go-ICP: A globally optimal solution to 3D ICP point-set registration," *IEEE Trans. Pattern Anal. Mach. Intell.*, vol. 38, no. 11, pp. 2241–2254, 2016.
- [18] A. P. Bustos, T. J. Chin, A. Eriksson, H. Li, and D. Suter, "Fast rotation search with stereographic projections for 3d registration," *IEEE Transactions on Pattern Analysis and Machine Intelligence*, vol. 38, no. 11, pp. 2227–2240, 2016.
- [19] B. Jian and B. C. Vemuri, "Robust point set registration using gaussian mixture models," *IEEE Transactions on Pattern Analysis and Machine Intelligence*, vol. 33, no. 8, pp. 1633–1645, 2011.
- [20] A. Myronenko and X. Song, "Point set registration: Coherent point drift," *IEEE Transactions on Pattern Analysis and Machine Intelligence*, vol. 32, no. 12, pp. 2262–2275, Dec 2010.
- [21] R. Horaud, F. Forbes, M. Yguel, G. Dewaele, and J. Zhang, "Rigid and articulated point registration with expectation conditional maximization," *IEEE Transactions on Pattern Analysis and Machine Intelligence*, vol. 33, no. 3, pp. 587–602, March 2011.
- [22] H. Mohammadzade and D. Hatzinakos, "Iterative closest normal point for 3D face recognition," *IEEE Transactions on Pattern Analysis and Machine Intelligence*, vol. 35, no. 2, pp. 381–397, 2013.
- [23] P. Heider, A. Pierre-Pierre, R. Li, and C. Grimm, "Local shape descriptors, a survey and evaluation," in *Proceedings of the EG 3DOR*. Aire-la-Ville, Switzerland: Eurographics, 2011, pp. 49–56.
- [24] T. Gatzke, C. Grimm, M. Garland, and S. Zelinka, "Curvature maps for local shape comparison," in *Proceedings of the International Conference on Shape Modeling and Applications*, ser. SMI '05. Washington, DC, USA: IEEE Computer Society, 2005, pp. 246–255.
- [25] N. Gelfand, N. J. Mitra, L. J. Guibas, and H. Pottmann, "Robust global registration," in *Proceedings of the Third Eurographics Symposium on Geometry Processing*, ser. SGP '05. Aire-la-Ville, Switzerland: Eurographics Association, 2005.
- [26] A. Tevs, A. Berner, M. Wand, I. Ihrke, and H.-P. Seidel, "Intrinsic shape matching by planned landmark sampling," vol. 30, no. 2. Blackwell Publishing Ltd, 2011, pp. 543–552.
- [27] L. Quan and K. Tang, "Polynomial local shape descriptor on interest points for 3D part-in-whole matching," *Computer-Aided Design*, vol. 59, pp. 119 – 139, 2015.
- [28] H. Wang, Y. K. Rong, H. Li, and P. Shaun, "Computer aided fixture design: Recent research and trends," *Computer-Aided Design*, vol. 42, no. 12, pp. 1085 – 1094, 2010.
- [29] I. Boyle, Y. Rong, and D. C. Brown, "A review and analysis of current computer-aided fixture design approaches," *Robotics and Computer-Integrated Manufacturing*, vol. 27, no. 1, pp. 1 – 12, 2011.
- [30] A. Nee, Z. Tao, and A. Kumar, *An Advanced Treatise On Fixture Design And Planning*, ser. Manufacturing Systems and Technology Series. World Scientific, 2004.
- [31] G.-F. Chen and L. Wen-jian, "Variant fixture design with CBR," in *Proceedings of International Conference on Machine Learning and Cybernetics*, vol. 3, 2002, pp. 1465–1469.
- [32] S. Vallapuzha, E. C. D. Meter, S. Choudhuri, and R. P. Khetan, "An investigation of the effectiveness of fixture layout optimization methods," *International Journal of Machine Tools and Manufacture*, vol. 42, no. 2, pp. 251 – 263, 2002.
- [33] Y. Chen and G. Medioni, "Object modelling by registration of multiple range images," *Image Vision Comput.*, vol. 10, no. 3, pp. 145–155, Apr. 1992.
- [34] Y. Zheng, M. Lin, and D. Manocha, "Efficient simplex computation for fixture layout design," *Computer-Aided Design*, vol. 43, no. 10, pp. 1307 – 1318, 2011, solid and Physical Modeling 2010.
- [35] I. Sipiran and B. Bustos, "A robust 3d interest points detector based on harris operator," in *Proceedings of the EG 3DOR*. Aire-la-Ville, Switzerland: Eurographics Association, 2010, pp. 7–14.
- [36] A. Godil and A. I. Wagan, "Salient local 3D features for 3D shape retrieval," vol. 7864, 2011, pp. 78 640S–8.
- [37] C. H. Lee, A. Varshney, and D. W. Jacobs, "Mesh saliency," *ACM Trans. Graph.*, vol. 24, no. 3, pp. 659–666, 2005.
- [38] U. Castellani, M. Cristani, S. Fantoni, and V. Murino, "Sparse points matching by combining 3d mesh saliency with statistical descriptors," *Comp. Grap. For.*, vol. 27, no. 2, pp. 643–652, 2008.
- [39] J. Novatnack and K. Nishino, "Scale-dependent 3d geometric features," in *IEEE ICCV*, 2007, pp. 1–8.
- [40] H. Meinzer, M. Fangerau, M. Schmidt, T. R. dos Santos, A. M. Franz, L. Maier-Hein, and J. M. Fitzpatrick, "Convergent iterative closest-point algorithm to accomodate anisotropic and inhomogeneous localization error," *IEEE Transactions on Pattern Analysis and Machine Intelligence*, vol. 34, no. 8, pp. 1520–1532, 2012.
- [41] S. Bouaziz, A. Tagliasacchi, and M. Pauly, "Sparse iterative closest point," in *Proceedings of the SGP*, ser. SGP '13. Aire-la-Ville, Switzerland: Eurographics Association, 2013, pp. 113–123.



Tsz-Ho Kwok is an Assistant Professor in the Department of Mechanical, Industrial and Aerospace Engineering at the Concordia University, Montreal, Canada. Before joining Concordia, he was a Postdoctoral Research Associate in the Epstein Department of Industrial and Systems Engineering at the University of Southern California. He received his Ph.D. degree in the Department of Mechanical and Automation Engineering from the Chinese University of Hong Kong. His research interests include 3D printing, design for additive manufacturing, functional design and fabrication, cyber-manufacturing system, and mass customization. Dr. Kwok has received several awards including the 8th Chinese Youth Science and Technology Innovation Prize, the Microsoft Research Fellowship Nomination Award, and the CUHK Postgraduate Research Output Award. He serves as an Associate Editor in the Transactions of the Canadian Society for Mechanical Engineering (TCSME).